iScience

CellPress
OPEN ACCESS

Article

Tailoring the amorphous Mo sites on layered double hydroxide nanosheets for nitrogen photofixation

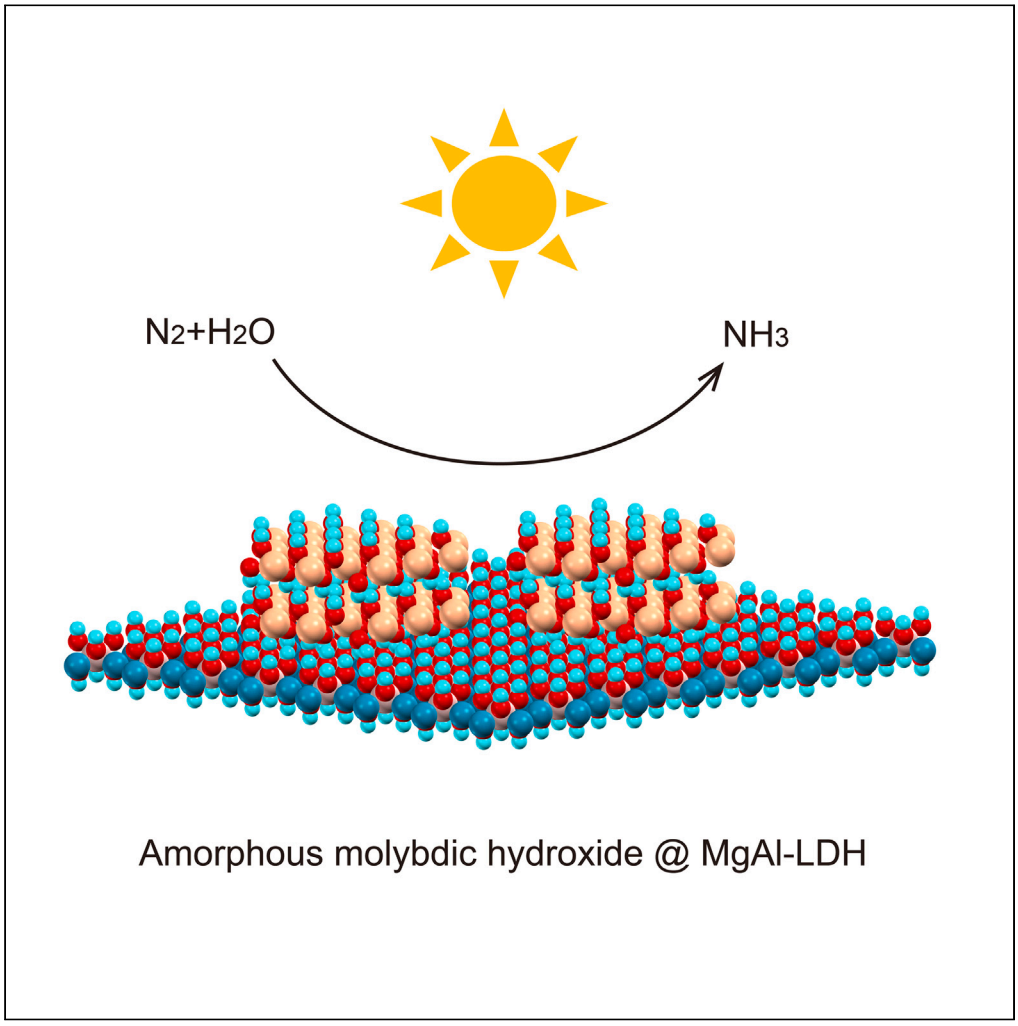

Jinhu Wang, Junyu Gao, Yingxuan Miao, Dong Li, Yunxuan Zhao, Tierui Zhang

yunxuan@mail.ipc.ac.cn (Y.Z.)
tierui@mail.ipc.ac.cn (T.Z.)

Highlights

The amorphous Mo@MgAl-LDH were synthesized by a facile coprecipitation strategy

Mo@MgAl-LDH can heighten the adsorption/activation of molecular N_2

Mo@MgAl-LDH demonstrates a considerable performance of nitrogen photofixation

Wang et al., iScience 27, 110088
June 21, 2024
https://doi.org/10.1016/j.isci.2024.110088

iScience

CellPress
OPEN ACCESS

Article

Tailoring the amorphous Mo sites on layered double hydroxide nanosheets for nitrogen photofixation

Jinhu Wang,[1,2] Junyu Gao,[1,2] Yingxuan Miao,[1,2] Dong Li,[1,2] Yunxuan Zhao,[1,*] and Tierui Zhang[1,2,3,*]

SUMMARY

While photocatalytic technology has brought additional opportunities and possibilities for the green conversion and sustainable development of ammonium-based nitrogen fertilizers, the low activation efficiency of the molecular N_2 has impeded its further application feasibility. Here to address the concern, we designed an amorphous molybdenum hydroxide anchored on the ultrathin magnesium-aluminum layered double hydroxide (Mo@MgAl-LDH) nanosheets for benefiting the N_2 photofixation to NH_3. With the aid of the designed amorphous Mo(V) species, the pristine MgAl-LDH exhibited a considerable performance of nitrogen photofixation under visible light irradiation (NH_3 production rate of 114.4 μmol g^{-1} h^{-1}) due to the improved N_2 activation efficiency. The work demonstrated a feasible strategy for nitrogen photofixation using amorphous Mo(V) species, which may also deliver a novel inspiration for the development of amorphous photocatalysts toward the photoactivation of molecular N_2.

INTRODUCTION

Ammonia (NH_3) serves as a pivotal feedstock in fertilizers, pharmaceuticals, and fine chemicals and holds promise as an ideal, carbon-free fuel.[1–3] Its significance in driving both agricultural and industrial development receiving widespread attention. Despite this, traditional industrial NH_3 production remains dominated by the Harber-Bosch process, necessitating high-purity nitrogen (N_2) and hydrogen streams subjected to demanding conditions (15–25 MPa, 400–500°C),[4] consuming *ca.* 2% of global energy.[5] In light of these challenges, there is a growing impetus to explore sustainable and eco-friendly strategies for NH_3 production, aligning with global objectives for carbon peaking and neutrality. Photocatalytic NH_3 production, leveraging the reduction of molecular N_2, emerges as a compelling alternative to the Harber-Bosch process. However, the obstinate N≡N triple bond (941 kJ mol^{-1}) driving low adsorption/activation efficiency impedes efficient NH_3 production.[2,6] Consequently, the pivot of constructing an economical photocatalytic NH_3 manufacturing system lies in augmenting N_2 activation efficiency.

Drawing insights from previous research regarding defect-rich semiconductor photocatalysts,[7] it becomes apparent that the unsaturated coordinated sites with low-valence metal species play a pivotal role in determining the adsorption and activation of molecular N_2. In particular, research on Mo(V)-containing compounds (such as Mo(V)/$W_{18}O_{49}$ and MoO_{3-x}) has begun to sprout in the field of N_2 photofixation.[8,9] Accordingly, there is considerable potential for coordinatively unsaturated Mo(V) species to function as crucial sites for N_2 adsorption/activation. Nevertheless, a substantial challenge arises from the inherent instability of low-valence Mo(V) species during photocatalytic reactions, leading to their transformation into Mo(VI) species.[10] Obviously, it is imperative to cultivate simpler and more efficient tactics for anchoring low-valence Mo(V) species on the substrates from the point of effective activation of molecular N_2, albeit technically challenging.

Layered double hydroxides (LDHs) are important members of two-dimensional nanomaterials with a general formula $[M^{2+}_{1-x}M^{3+}_{x}(OH)_2](A^{n-})_{x/n}\cdot yH_2O$, which offers a multi-functional platform for developing novel photocatalytic materials due to their controllable particle size, compositional flexibility, and facile synthesis.[11,12] Notably, the presence of HO-M-OH bridges provides a substrate for anchoring low-valence metal species onto the LDH laminates, as demonstrated in previous studies featuring ultrafine Cu_2O,[13] $Cu^{\delta+}$,[14] and ultrathin Ni/V[15] supported by LDHs. Hence, anchoring Mo(V) species on the LDH materials emerges as a potential strategy for stabilizing low-valence Mo(V) sites, which would be expected to enhance N_2 activation efficiency, thereby boosting photocatalytic NH_3 generation.

Herein, amorphous molybdenum hydroxide-anchored ultrathin MgAl-LDH (denoted as Mo@MgAl-LDH) nanosheets were successfully prepared by a facile coprecipitation method (Figure 1A). Furthermore, the existence of abundant unsaturated coordinated Mo species in as-designed Mo@MgAl-LDH was confirmed through various characterization techniques, including X-ray absorption fine structure (XAFS), X-ray photoelectron spectroscopy (XPS), high-resolution transmission electron microscopy (HRTEM), and thermogravimetric and differential

[1]Key Laboratory of Photochemical Conversion and Optoelectronic Materials, Technical Institute of Physics and Chemistry, Chinese Academy of Sciences, Beijing 100190, China
[2]Center of Materials Science and Optoelectronics Engineering, University of Chinese Academy of Sciences, Beijing 100049, China
[3]Lead contact
*Correspondence: yunxuan@mail.ipc.ac.cn (Y.Z.), tierui@mail.ipc.ac.cn (T.Z.)
https://doi.org/10.1016/j.isci.2024.110088

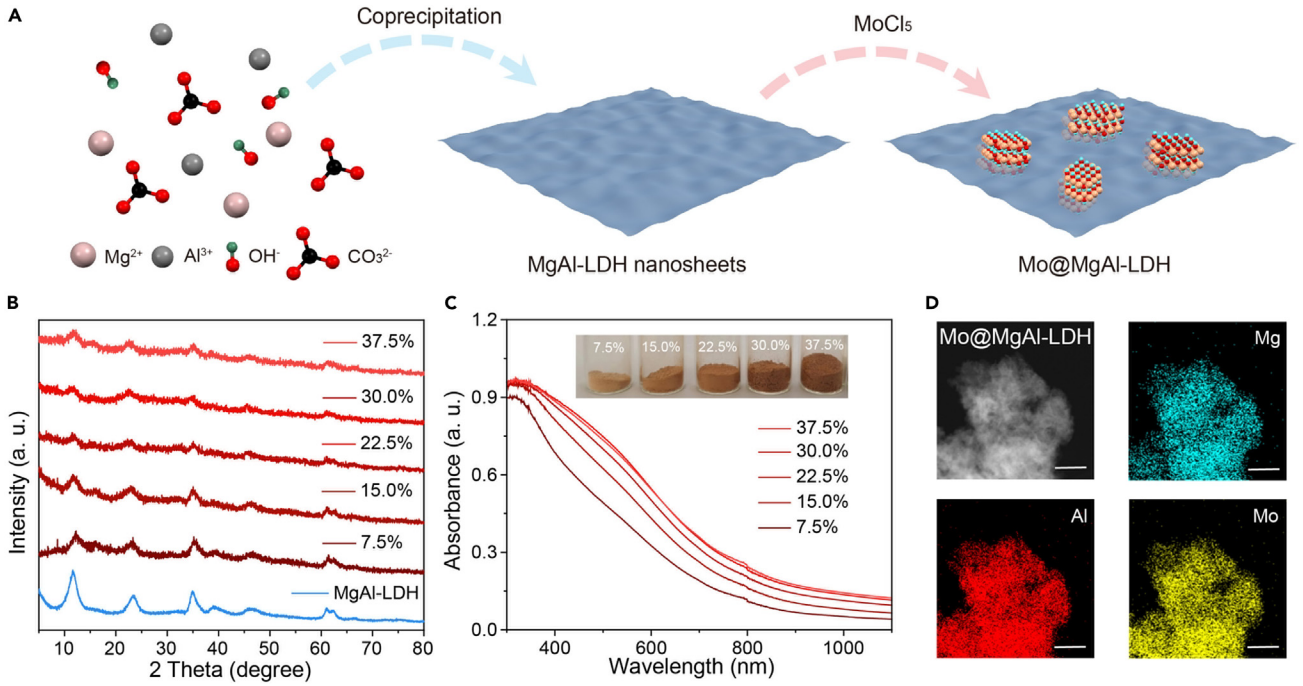

Figure 1. Structural characterizations of Mo@MgAl-LDH catalysts

(A) Schematic diagram of preparation for Mo@MgAl-LDH.

(B) XRD patterns, and (C) UV-vis DRS, for X-Mo@MgAl-LDH (X is 7.5, 15.0, 22.5, 30.0 and 37.5%) and MgAl-LDH.

(D) EDS element maps of 30%-Mo@MgAl-LDH (scale bar is 100 nm).

thermogravimetry (TG-DTG). Importantly, the as-prepared Mo@MgAl-LDH with abundant Mo sites can heighten the adsorption/activation of molecular N_2 and broaden the absorption spectrum in the visible region, thereby enhancing the performance of nitrogen photofixation relative to pristine MgAl-LDH nanosheets. Further, Mo@MgAl-LDH demonstrated substantial and enduring N_2-to-NH_3 performance in pure water under visible light irradiation, exhibiting a photocatalytic NH_3 evolution rate of 114.4 μmol g^{-1} h^{-1}. This finding derived from the as-prepared Mo@MgAl-LDH offers an additional consideration in the design of amorphous catalysts for nitrogen photofixation.

RESULTS AND DISCUSSION

Structural characterization of amorphous Mo@MgAl-LDH

Pristine ultrathin MgAl-LDH nanosheets were successfully synthesized through a coprecipitation method (full details are provided in the supplemental information). The crystal structure of MgAl-LDH nanosheets was confirmed *via* powder X-ray diffraction (XRD) patterns, which manifested characteristic (003), (006), (009), and (110) Bragg reflections consistent with conventional LDH structures (Figure S1).[16] Moreover, the ultrathin morphology of MgAl-LDH nanosheets was verified by TEM technology (Figure S2). Subsequently, the as-designed Mo@MgAl-LDH photocatalyst was obtained by incrementally adding a $MoCl_5$ solution to the liquid dispersion of MgAl-LDH (denoted herein as X-Mo@MgAl-LDH, where X = mol (Mo)/mol (Mg + Al) × 100%). The powder XRD patterns in Figure 1B for all the as-prepared X-Mo@MgAl-LDH samples exhibited typical Bragg reflections of MgAl-LDH structures, affirming the integration of amorphous Mo sites on the MgAl-LDH. To elucidate the transformation of amorphous Mo sites during the anchoring process, UV-vis diffuse reflectance spectra (UV-vis DRS) were systematically collected. Figure 1C illustrates that the absorption between 400 and 800 nm can be intensified with increasing X up to 30%, which is associated with amorphous Mo sites. The amorphous Mo(V) sites in the Mo@MgAl-LDH nanosheets can enhance the absorption intensity of UV-vis light for MgAl-LDH nanosheets. However, no significant alteration was observed upon further elevating X to 37.5% compared to pristine MgAl-LDH nanosheets (Figure S3). These outcomes implied that the optimal X could be 30% for the effective formation and augmentation of amorphous Mo sites anchored on the MgAl-LDH nanosheets (Mo@MgAl-LDH representing 30 mol% Mo anchored with the MgAl-LDH nanosheets).

To gain deeper insights into the structural features of the as-prepared Mo@MgAl-LDH, HRTEM imaging was employed. The presence of possibly amorphous Mo sites anchored on MgAl-LDH nanosheets was obtained through TEM images (Figure S4), aligning well with the observations from XRD patterns. Additionally, energy-dispersive spectrometry (EDS) mapping was conducted to thoroughly investigate the distribution of amorphous Mo sites on the Mo@MgAl-LDH. As depicted in Figure 1D, the measured results illustrate a uniform dispersion of Mo on the MgAl-LDH nanosheets, providing strong evidence for the successful anchoring of amorphous Mo sites on the MgAl-LDH nanosheets. Additionally, additional chemical composition analyses were performed using a field emission scanning electron microscope (SEM) equipped

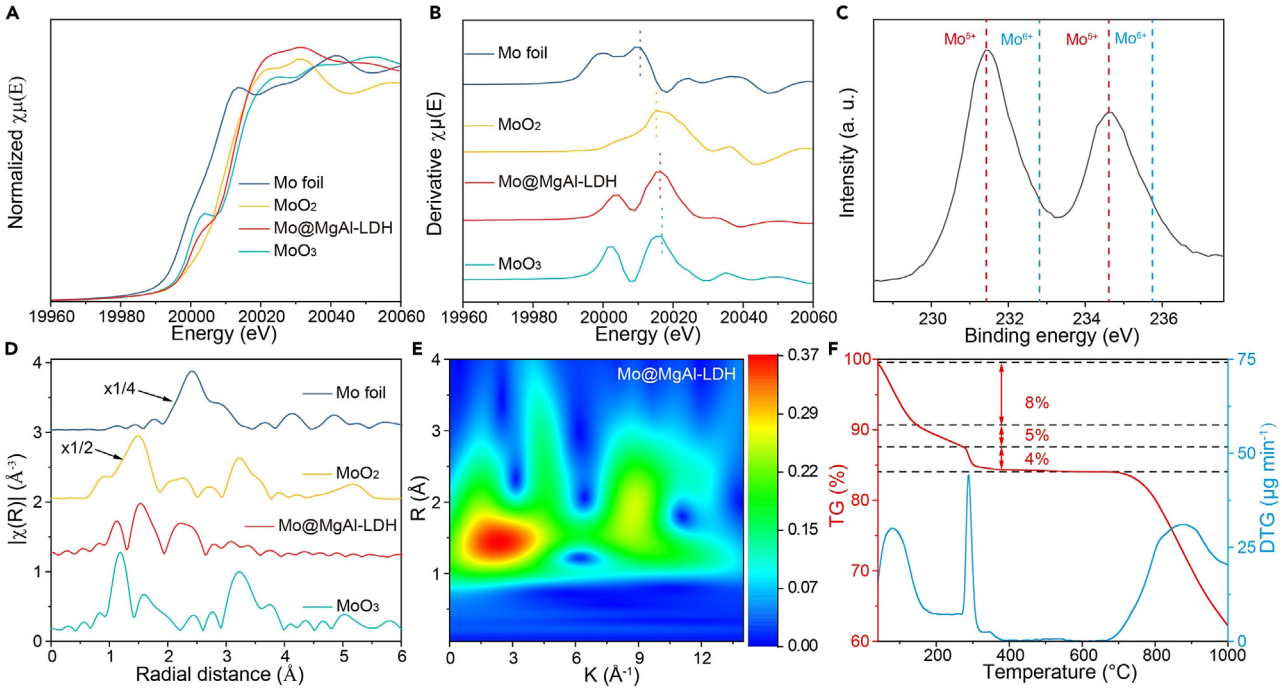

Figure 2. Structural characterizations of Mo@MgAl-LDH catalyst

(A) Mo K-edge XANES spectra of amorphous Mo@MgAl-LDH and standard Mo foil, MoO_2, and MoO_3 samples.

(B) XAFS spectra first derivative of amorphous Mo@MgAl-LDH and standard Mo foil, MoO_2, and MoO_3 samples.

(C) XPS spectrum for the Mo 3d region of amorphous Mo@MgAl-LDH.

(D) EXAFS spectra of amorphous Mo@MgAl-LDH and standard Mo foil, MoO_2, and MoO_3 samples at Mo K-edge.

(E) Wavelength transform analyses of EXAFS of amorphous Mo@MgAl-LDH.

(F) TG and DTG plot of hydrolysis product for molybdenum(V) chloride without MgAl-LDH.

with EDS elemental analysis capabilities. The actual contents of Mo in as-prepared Mo@MgAl-LDH are determined quantitatively by the EDS mapping (Figure S5 and Table S1). It is calculated that its experimental value (27.9%) decreased (Table S1), compared to 30%-Mo@MgAl-LDH, when the theoretical value of the molar ratio (mol (Mo)/mol (Mg + Al) × 100%) reaches 37.5% for Mo@MgAl-LDH. Further insights into the valence state and coordination environment of Mo species within the amorphous Mo@MgAl-LDH nanosheets were garnered through XPS and XAFS analyses. Figure S6 presented XPS datum of amorphous Mo@MgAl-LDH, revealing the prevalent existence of Mo(V) species in the as-prepared amorphous Mo@MgAl-LDH nanosheets, consistent with the findings from EDS mapping.[17] Moreover, XAFS spectra were collected to offer a comprehensive understanding of the electronic structure and coordination environment of the amorphous Mo species. As shown in Figure 2A, the elemental valence state of Mo in Mo@MgAl-LDH was scrutinized using X-ray absorption near edge structure (XANES) at the Mo K-edge. The position of the edge in Mo@MgAl-LDH was found to be intermediate between MoO_2 and MoO_3, suggesting that the valence state of Mo falls within the range of +4.0 to +6.0. Furthermore, the first derivative of the XANES spectra for reference samples (Mo foil, MoO_2, and MoO_3) serves as compelling evidence for the intermediate oxidation state of Mo, consistent with the findings from XPS analysis (Figures 2B and 2C).

Figure 2D displayed the Fourier transform k_2-weighted extended X-ray absorption fine structure (EXAFS) spectra of the amorphous Mo@MgAl-LDH and reference samples (Mo foil, MoO_3, and MoO_2) at the Mo K-edge. The EXAFS spectra provided intricate details regarding the Mo-O coordination shell in the amorphous Mo@MgAl-LDH. A notable feature is the conspicuous discrepancy in peak intensities within the EXAFS spectra of amorphous Mo@MgAl-LDH and MoO_3 samples, indicating a significant shift in the peaks of Mo-O shells within the range of 1–2 Å, as opposed to other shells. The characteristic peaks at approximately 1.1 Å and 1.6 Å can be attributed to the contributions of Mo-O shells, respectively.[18] For a more nuanced understanding of the atomic separation distances between Mo and O atoms, wavelet transform analyses of the four samples were conducted during the visualization process (Figure 2E). From the aforementioned results, two coordination environments similar to molybdenum hydroxide and molybdenum oxide may be presented in the amorphous Mo@MgAl-LDH nanosheets. To discern these amorphous Mo(V) sites, TG-DTG was conducted over the temperature range of 18°C–1000°C. Figure 2F depicts the TG-DTG curve of the synthesized amorphous Mo(V) sites after etching MgAl-LDH, revealing well-defined decomposition ranges. The TG profile displayed two main regions within the temperature ranges of 18°C–270°C and 270°C–500°C. The initial weight loss (18°C–270°C) was attributed to the physisorption and the initial dehydration of the amorphous Mo(V) sites. Subsequently, the weight loss between 280°C and 500°C, accounting for approximately 4%, could be ascribed to the secondary dehydration of the amorphous Mo(V) sites. Over this temperature range,

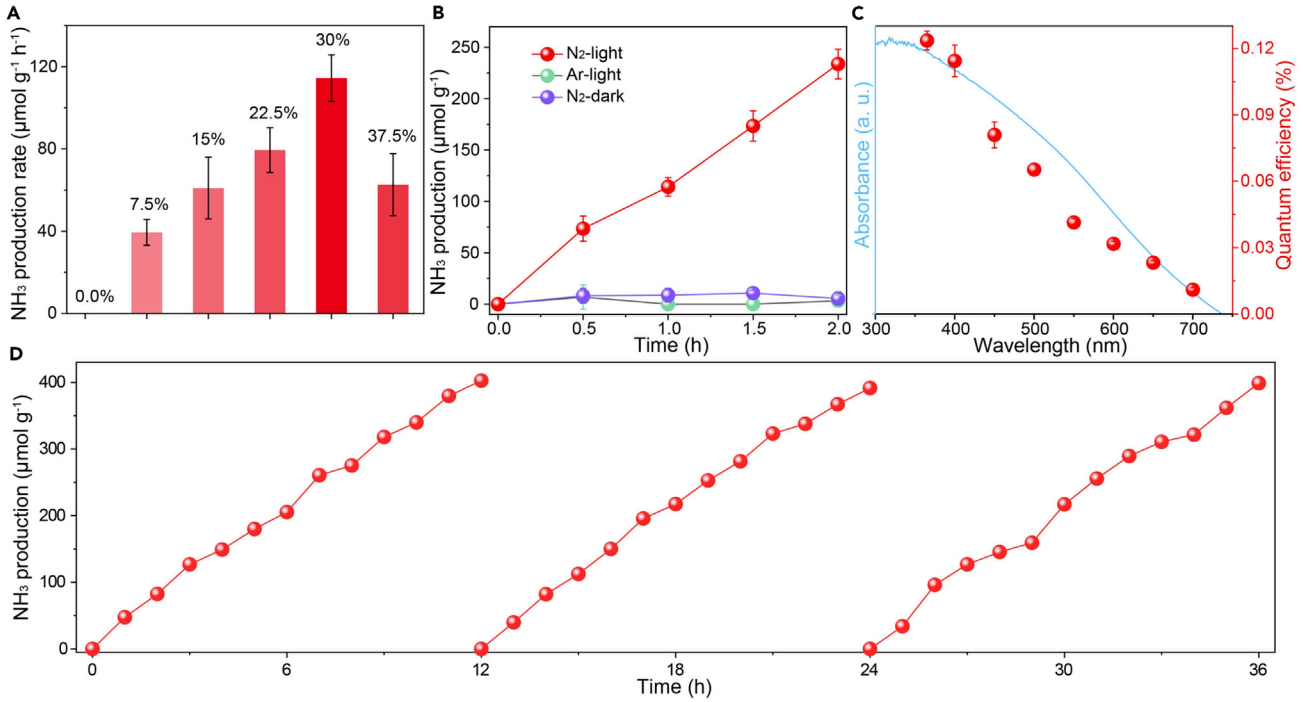

Figure 3. Photocatalytic NH_3 production of Mo@MgAl-LDH

(A) Photocatalytic NH_3 production rate for X-Mo@MgAl-LDH (X = 0, 7.5, 15%, 22.5%, 30%, and 37.5%) in N_2-saturated water under 2 h of visible light irradiation.

(B) Time course study of photocatalytic N_2 reduction and various control experiments over Mo@MgAl-LDH.

(C) Wavelength-dependent apparent AQE for N_2 photoreduction and (D) cycling test data in N_2-saturated water under visible light irradiation over Mo@MgAl-LDH. The error bars were obtained by calculating the standard deviation from two parallel experiments.

the LDH underwent dehydroxylation reactions, yielding metal oxides in accordance with prior reports.[19,20] Notably, a major endothermic peak around 80°C was observed, primarily associated with physisorption and dehydroxylation reactions, suggesting a substantial overlap. Additionally, the endothermic peak around 290°C and the broad endothermic peak around 80°C in the TG-DTG curves may be indicative of dehydration and dehydroxylation processes.[20] Results indicated that the amorphous Mo(V) sites in Mo@MgAl-LDH would be hydroxide, rather than molybdenum oxide.

Performance of photocatalytic nitrogen reduction to ammonia

Building upon the successful anchoring of amorphous Mo(V) on MgAl-LDH nanosheets, we conducted a comprehensive evaluation of their photocatalytic performance in the conversion of N_2 into NH_3 under visible irradiation (400–800 nm). The quantification of produced NH_3 was carried out using ion chromatography (Figure S7). Figure 3A illustrated the NH_3 generation rates in the following order: 30%-Mo@MgAl-LDH (114.4 μmol g^{-1} h^{-1}) > 22.5%-Mo@MgAl-LDH (79.5 μmol g^{-1} h^{-1}) > 37.5%-Mo@MgAl-LDH (62.6 μmol g^{-1} h^{-1}) > 15%-Mo@MgAl-LDH (61.0 μmol g^{-1} h^{-1}) > 7.5%-Mo@MgAl-LDH (39.5 μmol g^{-1} h^{-1}) > molybdenum hydroxide (1.1 μmol g^{-1} h^{-1}) > MgAl-LDH (0.8 μmol g^{-1} h^{-1}) (Figures S8–S12). This trend aligns with the absorption intensity of light in the visible light region. Moreover, it can be seen that when the experimental value of the molar ratio (mol (Mo)/mol (Mg + Al) × 100%) reaches 27.9%, NH_3 generation rates decreased, compared to 30%. This exception may be that 37.5% exceeds the maximum number of anchored molybdenum sites on MgAl-LDH. The redundant Mo species without anchored on the MgAl-LDH agglomerated into large particles (Figure S8), which reduced the performance of photocatalytic NH_3 production. Remarkably, amorphous Mo@MgAl-LDH exhibited a noteworthy photocatalytic NH_3 production rate surpassing most reported LDH-based photocatalysts (refer to Table S2), underscoring its exceptional photocatalytic activity. Additionally, control experiments conducted under Ar bubbling (300 mL min^{-1}) or without light illumination using amorphous Mo@MgAl-LDH resulted in negligible ammonia generation (Figure 3B). Conversely, a clear positive correlation was observed between photocatalytic NH_3 production concentration and illumination time under visible light and N_2 atmosphere. These results confirmed the considerable efficacy of amorphous Mo sites in nitrogen photofixation.

Moreover, we conducted measurements of apparent quantum efficiency (AQE) to quantify the efficiency of the photocatalytic process. The calculated AQEs were determined to be 0.12% at 365 nm, 0.12% at 400 nm, 0.08% at 450 nm, 0.06% at 500 nm, 0.04% at 550 nm, 0.03% at 600 nm, 0.02% at 650 nm, and 0.01% at 700 nm (Figure 3C). A discernible correlation was observed between the trend of AQE variation and the absorption spectrum of amorphous Mo@MgAl-LDH, providing substantial evidence for the role of visible light in energizing electrons for photocatalytic NH_3 production. Furthermore, the stability of amorphous Mo@MgAl-LDH for photocatalytic NH_3 production was

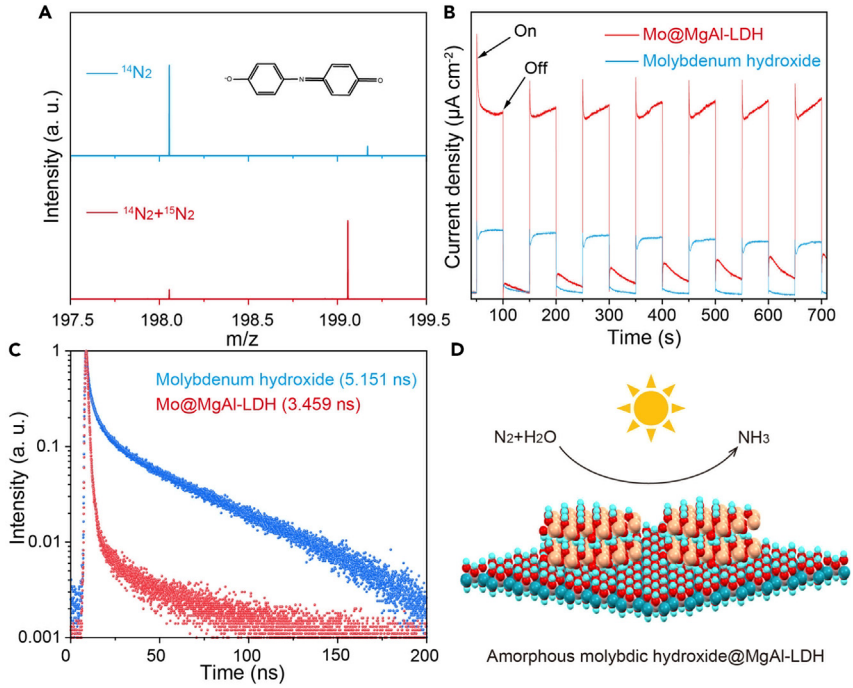

Figure 4. Isotope experiments and photodynamics analyses

(A) Mass spectra of the products formed via reaction with indophenol following photocatalysis in different reaction atmospheres (the inset shows the chemical structure of the products formed by the indophenol blue method).

(B) Photocurrent responses under UV-vis light illumination.

(C) Time-resolved photoluminescence decay curves.

(D) Scheme for photocatalytic N_2 fixation process on the surface of amorphous Mo@MgAl-LDH.

evaluated, with negligible changes in performance during cycling tests (Figure 3D). Photocatalytic NH_3 production is susceptible to the presence of ambient nitrogen-containing species. To confirm that the nitrogen source of the generated NH_3 exclusively originated from molecular N_2, a series of meticulously isotope experiments were conducted using various feed gases ($^{14}N_2$ and $^{15}N_2$). The obtained product, $^{15}NH_4^+$, was detected using the indophenol blue method and further analyzed by high-resolution mass spectroscopy. As depicted in Figure 4A, the product solution obtained using $^{15}N_2$ as the reactant exhibited a distinct mass spectroscopy peak at 199.0585 (m/z).[13,16] Furthermore, the $^{15}N/^{14}N$ abundance ratio was notably higher when $^{15}N_2$ was used as the nitrogen source compared to $^{14}N_2$. These experiments conclusively confirmed that N_2 was indeed the exclusive source of NH_3 evolved during the photocatalytic tests. Additionally, quantitative determination of potential byproducts (NO_3^-, NO_2^-, and N_2H_4) was performed using the ion chromatography method and dimethylaminobenzaldehyde spectrophotometry with standard curves. Notably, no significant amounts of NO_3^-, NO_2^-, H_2, or N_2H_4 can be detected,[21] demonstrating a high selectivity for N_2 reduction to NH_3 (Figures S13–S15).

Photodynamics analyses of amorphous Mo@MgAl-LDH

In order to investigate the photoinduced charge transfer mechanism underlying photocatalytic NH_3 production, we conducted photocurrent and time-resolved photoluminescence decay measurements using amorphous Mo@MgAl-LDH and molybdenum hydroxide. The data presented in Figure 4B illustrated that the photocurrent density of amorphous Mo@MgAl-LDH significantly surpassed that of amorphous molybdenum hydroxide, indicating an enhanced separation and transfer efficiency of electrons and holes in amorphous Mo@MgAl-LDH following photoexcitation. The electrochemical impedance spectroscopy testing of MgAl-LDH and Mo@MgAl-LDH to further confirm efficient electron transfer in Mo@MgAl-LDH nanosheets (Figure S16). To track the pathway of the photo-induced electron and hole for Mo@MgAl-LDH, Mott-Schottky curves were collected to obtain the flat band potentials for Mo@MgAl-LDH. The flat band potential of amorphous Mo@MgAl-LDH was calculated to be −0.013 V versus the normal hydrogen electrode (NHE) (Figure S17).[22,23] Moreover, the band gap was explored through Tauc's plots derived from the UV-vis DRS. From the UV-vis DRS measurements (Figure S18), the bandgap for the amorphous Mo@MgAl-LDH nanosheets was estimated to be ≈ 2.12 eV *vs.* NHE.[23] Combining insights from UV-vis DRS and MS plots, the bandgap of Mo@MgAl-LDH was calculated and depicted in nitrogen photofixation (Figure S19). To further verify the previous deductions, photoluminescence decay and time-resolved photoluminescence decay experiments were conducted for amorphous Mo@MgAl-LDH and molybdenum hydroxide (Figures S20 and S21). As shown in Figure 4C, the amorphous molybdenum hydroxide had longer average decay times (*ca.* 5.151 ns) compared with amorphous Mo@MgAl-LDH (*ca.* 3.459 ns) (Table S3), demonstrating that Mo sites would act as trapping sites for improving photogenerated

transfer efficiency of charge carriers (Figure S22).[16,24] The data indicated that Mo-anchored ultrathin MgAl-LDH facilitated the effective separation of electron-hole pairs compared to the molybdenum hydroxide, leading to enhanced nitrogen activation efficiency, together with high photocatalytic NH_3 production rates. Consequently, we demonstrated that the amorphous Mo sites anchored on ultrathin MgAl-LDH nanosheets can be solidly maintained as low-valance Mo and strong light utilization efficiency, resulting in a substantial improvement in N_2 photofixation performance under visible-light irradiation (Figures 4D and S23).[25]

DISCUSSION

In summary, we successfully prepared a Mo@MgAl-LDH photocatalyst using a facile coprecipitation strategy. The detailed constructions of molybdenum hydroxide-anchored ultrathin MgAl-LDH nanosheets were analyzed through XRD, TEM, XAFS, and TG-DTG. The measured results collectively affirmed the stable anchoring of low-valence amorphous Mo sites on the ultrathin MgAl-LDH nanosheets. Additionally, as evidenced by UV-vis DRS, Mo@MgAl-LDH exhibited robust light utilization efficiency, resulting in a significant photocatalytic NH_3 production rate (114.4 $\mu mol\ g^{-1}\ h^{-1}$) in pure water under visible light irradiation. This finding, stemming from the characteristics of the as-prepared Mo@MgAl-LDH nanosheets, introduces a new idea for the development of amorphous catalysts for nitrogen photofixation.

Limitations of the study

The construction of Mo species is difficult to identify and construct due to its amorphous characteristic.

STAR★METHODS

Detailed methods are provided in the online version of this paper and include the following:

- KEY RESOURCES TABLE
- RESOURCE AVAILABILITY
  - Lead contact
  - Materials availability
  - Data and code availability
- METHOD DETAILS
  - Materials
  - Synthesis of MgAl-LDH
  - Synthesis of Mo@MgAl-LDH
  - Synthesis of molybdenum hydroxide
  - Materials characterizations
  - Photocatalytic N_2 reduction tests
  - The apparent quantum efficiency tests
  - Photocatalytic N_2 reduction cycling tests
  - Isotopic labeling experiments
  - Photoelectrochemical measurements
  - Gibbs free energy calculations of nitrogen photofixation to ammonia

SUPPLEMENTAL INFORMATION

Supplemental information can be found online at https://doi.org/10.1016/j.isci.2024.110088.

ACKNOWLEDGMENTS

The authors are grateful for financial support from the National Key R&D Program of China (2023YFA1507202), the National Natural Science Foundation of China (51825205, 52120105002, 22322905, 22102202, 22088102, U22A20391), the DNL Cooperation Fund, CAS (DNL202016), and the CAS Project for Young Scientists in Basic Research (YSBR-004). The XAFS experiments were conducted in 1W1B beamline of Beijing Synchrotron Radiation Facility (BSRF).

AUTHOR CONTRIBUTIONS

J.W., Y.Z., and T.Z. conceived the idea for the project. Y.Z. and T.Z. supervised the project. J.W., Y.Z., J.G., Y.M., and D.L. conducted the measurement and characterizations. J.W., Y.Z., and T.Z. wrote the manuscript. All authors discussed the results and commented on the manuscript at all stages.

DECLARATION OF INTERESTS

The authors declare no competing interests.

Received: February 24, 2024
Revised: March 27, 2024
Accepted: May 20, 2024
Published: May 22, 2024

REFERENCES

1. Comer, B.M., Fuentes, P., Dimkpa, C.O., Liu, Y.H., Fernandez, C.A., Arora, P., Realff, M., Singh, U., Hatzell, M.C., and Medford, A.J. (2019). Prospects and challenges for solar fertilizers. Joule *3*, 1578–1605. https://doi.org/10.1016/j.joule.2019.05.001.
2. Yang, K., Han, S., Wang, Y., Zhang, B., and Yu, Y. (2023). Sustainable production and in-place utilization of a liquid nitrogenous fertilizer. Joule *7*, 1948–1955. https://doi.org/10.1016/j.joule.2023.07.020.
3. Chen, J.G., Crooks, R.M., Seefeldt, L.C., Bren, K.L., Bullock, R.M., Darensbourg, M.Y., Holland, P.L., Hoffman, B., Janik, M.J., Jones, A.K., et al. (2018). Beyond fossil fuel-driven nitrogen transformations. Science *360*, eaar6611. https://doi.org/10.1126/science.aar6611.
4. Kandemir, T., Schuster, M.E., Senyshyn, A., Behrens, M., and Schlögl, R. (2013). The Haber-Bosch process revisited: on the real structure and stability of "ammonia iron" under working conditions. Angew. Chem. Int. Ed. *52*, 12723–12726. https://doi.org/10.1002/anie.201305812.
5. Wang, L., Xia, M., Wang, H., Huang, K., Qian, C., Maravelias, C.T., and Ozin, G.A. (2018). Greening ammonia toward the solar ammonia refinery. Joule *2*, 1055–1074. https://doi.org/10.1016/j.joule.2018.04.017.
6. Hu, C., Chen, X., Jin, J., Han, Y., Chen, S., Ju, H., Cai, J., Qiu, Y., Gao, C., Wang, C., et al. (2019). Surface plasmon enabling nitrogen fixation in pure water through a dissociative mechanism under mild conditions. J. Am. Chem. Soc. *141*, 7807–7814. https://doi.org/10.1021/jacs.9b01375.
7. Shi, R., Zhao, Y., Waterhouse, G.I.N., Zhang, S., and Zhang, T. (2019). Defect engineering in photocatalytic nitrogen fixation. ACS Catal. *9*, 9739–9750. https://doi.org/10.1021/acscatal.9b03246.
8. Zhang, N., Jalil, A., Wu, D., Chen, S., Liu, Y., Gao, C., Ye, W., Qi, Z., Ju, H., Wang, C., et al. (2018). Refining defect states in $W_{18}O_{49}$ by Mo doping: a strategy for tuning N_2 activation towards solar-driven nitrogen fixation. J. Am. Chem. Soc. *140*, 9434–9443. https://doi.org/10.1021/jacs.8b02076.
9. Bai, H., Lam, S.H., Yang, J., Cheng, X., Li, S., Jiang, R., Shao, L., and Wang, J. (2022). A Schottky-barrier-free plasmonic semiconductor photocatalyst for nitrogen fixation in a "one-stone-two-birds" manner. Adv. Mater. *34*, 2104226. https://doi.org/10.1002/adma.202104226.
10. Zhang, S., Zhao, Y., Shi, R., Waterhouse, G.I., and Zhang, T. (2019). Photocatalytic ammonia synthesis: recent progress and future. EnergyChem *1*, 100013. https://doi.org/10.1016/j.enchem.2019.100013.
11. Yu, J., Wang, Q., O'Hare, D., and Sun, L. (2017). Preparation of two dimensional layered double hydroxide nanosheets and their applications. Chem. Soc. Rev. *46*, 5950–5974. https://doi.org/10.1039/C7CS00318H.
12. Wang, Q., and O'Hare, D. (2012). Recent advances in the synthesis and application of layered double hydroxide (LDH) nanosheets. Chem. Rev. *112*, 4124–4155. https://doi.org/10.1021/cr200434v.
13. Zhang, S., Zhao, Y., Shi, R., Zhou, C., Waterhouse, G.I.N., Wang, Z., Weng, Y., and Zhang, T. (2021). Sub-3 nm ultrafine Cu_2O for visible light driven nitrogen fixation. Angew. Chem. Int. Ed. *60*, 2554–2560. https://doi.org/10.1002/anie.202013594.
14. Zhang, S., Zhao, Y., Shi, R., Zhou, C., Waterhouse, G.I.N., Wu, L., Tung, C., and Zhang, T. (2020). Efficient photocatalytic nitrogen fixation over $Cu^{\delta+}$-modified defective ZnAl-layered double hydroxide nanosheets. Adv. Energy Mater. *10*, 1901973. https://doi.org/10.1002/aenm.201901973.
15. Liu, X., Li, Y., Zhang, J., and Lu, J. (2021). Ultrathin Ni/V-layered double hydroxide nanosheets for efficient visible-light-driven photocatalytic nitrogen reduction to ammonia. Nano Res. *14*, 3372–3378. https://doi.org/10.1007/s12274-021-3641-3.
16. Zhao, Y., Zheng, L., Shi, R., Zhang, S., Bian, X., Wu, F., Cao, X., Waterhouse, G.I.N., and Zhang, T. (2020). Alkali etching of layered double hydroxide nanosheets for enhanced photocatalytic N_2 reduction to NH_3. Adv. Energy Mater. *10*, 2002199. https://doi.org/10.1002/aenm.202002199.
17. De Castro, I.A., Datta, R.S., Ou, J.Z., Castellanos-Gomez, A., Sriram, S., Daeneke, T., and Kalantar-zadeh, K. (2017). Molybdenum oxides-from fundamentals to functionality. Adv. Mater. *29*, 1701619. https://doi.org/10.1002/adma.201701619.
18. Yin, H., Chen, Z., Peng, Y., Xiong, S., Li, Y., Yamashita, H., and Li, J. (2022). Dual active centers bridged by oxygen vacancies of ruthenium single-atom hybrids supported on molybdenum oxide for photocatalytic ammonia synthesis. Angew. Chem. Int. Ed. *61*, e202114242. https://doi.org/10.1002/anie.202114242.
19. Millange, F., Walton, R.I., and O'Hare, D. (2000). Time-resolved in situ X-ray diffraction study of the liquid-phase reconstruction of Mg-Al-carbonate hydrotalcite-like compounds. J. Mater. Chem. *10*, 1713–1720. https://doi.org/10.1039/B002827O.
20. Matsuda, K., Iio, N., Kawashimo, M., Okuda, A., Fukuzaki, R., Tarutani, N., Katagiri, K., and Inumaru, K. (2023). Comprehensive analysis of the chemical and structural transformations of Mg-Al-CO_3 layered double hydroxides with different Mg/Al ratios at elevated temperatures. Inorg. Chem. *62*, 17276–17287. https://doi.org/10.1021/acs.inorgchem.3c02571.
21. Bian, X., Zhao, Y., Zhang, S., Li, D., Shi, R., Zhou, C., Wu, L.Z., and Zhang, T. (2021). Enhancing the supply of activated hydrogen to promote photocatalytic nitrogen fixation. ACS Mater. Lett. *3*, 1521–1527. https://doi.org/10.1021/acsmaterialslett.1c00504.
22. Yang, H., Hou, H., Yang, M., Zhu, Z., Fu, H., Zhang, D., Luo, Y., and Yang, W. (2023). Engineering the S-scheme heterojunction between NiO microrods and MgAl-LDH nanoplates for efficient and selective photoreduction of CO_2 to CH_4. Chem. Eng. J. *474*, 145813. https://doi.org/10.1016/j.cej.2023.145813.
23. Chen, J., Wang, C., Zhang, Y., Guo, Z., Luo, Y., and Mao, C.J. (2020). Engineering ultrafine NiS cocatalysts as active sites to boost photocatalytic hydrogen production of MgAl layered double hydroxide. Appl. Surf. Sci. *506*, 144999. https://doi.org/10.1016/j.apsusc.2019.144999.
24. Du, S., Lian, J., and Zhang, F. (2022). Visible light-responsive N-doped TiO_2 photocatalysis: synthesis, characterizations, and applications. Trans. Tianjin Univ. *28*, 33–52. https://doi.org/10.1007/s12209-021-00303-w.
25. Ling, C., Niu, X., Li, Q., Du, A., and Wang, J. (2018). Metal-free single atom catalyst for N_2 fixation driven by visible light. J. Am. Chem. Soc. *140*, 14161–14168. https://doi.org/10.1021/jacs.8b07472.

STAR★METHODS

KEY RESOURCES TABLE

REAGENT or RESOURCE	SOURCE	IDENTIFIER
Chemicals		
$MoCl_5$ (99.95 wt.%)	Aladdin	CAS: 10241-05-1
H_2SO_4 (98 wt.%)	Aladdin	CAS: 7664-93-9
NaOH (98 wt.%)	Aladdin	CAS: 1310-73-2
NaClO (98 wt.%)	Aladdin	CAS: 7681-52-9
$NH_3{\cdot}H_2O$ (25–28 wt.%)	Aladdin	CAS: 1336-21-6
Na_2SO_4 (99 wt.%)	Innochem	CAS: 7757-82-6
$MgSO_4{\cdot}6H_2O$ (99 wt.%)	Innochem	CAS: 17830-18-1
$Al_2(SO_4)_3{\cdot}9H_2O$ (99 wt.%)	Innochem	CAS: 7784-31-8
Na_2CO_3 (99 wt.%)	Innochem	CAS: 497-19-8
α-terpineol (AR-grade)	Innochem	CAS: 10482-56-1
Trisodium citrate dihydrate (HPLC-grade)	Innochem	CAS: 6132-04-3
Phenol (HPLC-grade)	Innochem	CAS: 108-95-2
Ethanol (AR-grade)	Aladdin	CAS: 64-17-5
Paradimethylaminobenzaladehyde (AR-grade)	Aladdin	CAS: 100-10-7
Ethyl cellulose ether (CP-grade)	Aladdin	CAS: 9004-57-3
Sodium nitroprusside (AR-grade)	Aladdin	CAS: 14402-89-2
Gases		
N_2 (99.999%)	Beijing Qianxi Gases Company	CAS: 7727-37-9
Ar (99.999%)	Beijing Qianxi Gases Company	CAS: 7440-37-1
$^{15}N_2$ (99 atom% ^{15}N)	Aladdin	CAS: 29817-79-6

RESOURCE AVAILABILITY

Lead contact

Further information and requests for resources should be directed to and will be fulfilled by the lead contact, Tierui Zhang (tierui@mail.ipc.ac.cn).

Materials availability

All materials generated in this study are available from the lead contact without restriction.

Data and code availability

- The data supporting this study's findings are available from the lead contact upon reasonable request.
- This paper does not report the original code.
- Any additional information required to reanalyze the data reported in this paper is available from the lead contact upon request.

METHOD DETAILS

Materials

$MoCl_5$ (99.95 wt.%), H_2SO_4 (98 wt.%), NaOH (98 wt.%), NaClO (98 wt.%), and $NH_3{\cdot}H_2O$ (25–28 wt.%) were purchased from Aladdin. Na_2SO_4 (99 wt.%), $MgSO_4{\cdot}6H_2O$ (99 wt.%), $Al_2(SO_4)_3{\cdot}9H_2O$ (99 wt.%), Na_2CO_3 (99 wt.%), α-terpineol (AR-grade), trisodium citrate dihydrate (HPLC-grade), and phenol (HPLC-grade) were obtained from Innochem. Ethanol (AR-grade), paradimethylaminobenzaladehyde (AR-grade), ethyl cellulose ether (CP-grade), and sodium nitroprusside (AR-grade) were purchased from Aladdin. N_2 (99.999%) and Ar (99.999%) were obtained from the Beijing Qianxi Gases Company. Ultra-pure water was used in all experiments. $^{15}N_2$ was purchased from Aladdin. All chemicals were of analytical/HPLC grade and used as received without further purification.

Synthesis of MgAl-LDH

Solution A: aqueous solutions containing $MgSO_4 \cdot 6H_2O$ (0.08 mol) and $Al_2(SO_4)_3 \cdot 9H_2O$ (0.04 mol) with a Mg^{2+}/Al^{3+} molar ratio of 2.0 were prepared by dissolving the metal salts in deionized water (60 mL). Solution B was prepared by dissolving NaOH (0.24 mol) and Na_2CO_3 (0.2 mol) in deionized water (80 mL). Then, solution B was added dropwise into solution A under constant stirring. The solid product obtained was collected by centrifugation, washed several times with deionized water and then dried at −52 ∼ -47°C (freeze drying) under vacuum for 24 h.

Synthesis of Mo@MgAl-LDH

Solution A: aqueous solutions containing MgAl-LDH (4.2 g) with a Mg^{2+}/Al^{3+} molar ratio of 2.0 were prepared by dissolving the metal salts in deionized water (100 mL). Solution B was prepared by dissolving $MoCl_5$ (220 mmol L^{-1}, 100 mL)) in deionized water. Then, solution A (20 mL) was added dropwise into solution B (20 mL, c = 44, 88, 132, 176, and 220 mmol L^{-1}) under constant stirring. The solid product obtained was collected by centrifugation, washed several times with deionized water, and then dried at −52 ∼ -47°C (freeze drying) under vacuum for 24 h.

Synthesis of molybdenum hydroxide

Briefly, 2 g of $MoCl_5$ powder was dispersed into 100 mL of deionized water (solution A). Simultaneously, 2 g of NaOH was dissolved into 50 mL of deionized water (solution B). Solution B was then added dropwise into solution A under constant stirring. Until pH = 7 of mixed solution, the solid product obtained was collected by centrifugation, washed several times with deionized water and then dried at −52 ∼ -47°C (freeze drying) under vacuum for 24 h.

Materials characterizations

X-ray diffraction (XRD) patterns were recorded using a Bruker D8 Focus X-ray diffractometer equipped with a Cu Kα radiation source. The transmission electron microscopy (TEM) and high-resolution TEM (HRTEM) images were taken with the JEOL-2100F microscope. The instrument is also equipped with high-angle annular dark-field scanning TEM (HAADF-STEM) and energy-dispersive X-ray (EDX) elemental mapping. The scanning electron microscopy (SEM) images were observed by S-4800 at an operating voltage of 10 kV (Hitachi, Japan) equipped with energy dispersive spectrometry (EDS) elemental analyses capabilities. Ultraviolet-visible diffuse reflectance spectra (UV-vis DRS) were conducted across the wavelength range of 200–2500 nm on an Agilent Technologies Cary 7000 spectrometer. X-ray photoelectron spectroscopy (XPS) was acquired on an ESCALAB 250Xi spectrometer. For the XPS analysis, binding energies were calibrated against the C1s signal of adventitious hydrocarbons (284.8 eV). Mo K-edge X-ray absorption fine structure measurements were carried out on the 1W1B beamline at the Beijing Synchrotron Radiation Facility.

Photocatalytic N_2 reduction tests

The photocatalytic N_2 reduction performance of Mo@MgAl-LDH was assessed under vis-NIR light irradiation, utilizing a 300 W Xe lamp (PLS-SXE300DUV) with a 400 nm cutoff filter to simulate vis-NIR light (> 400 nm, light intensity of 1.3 W cm^{-2}). Prior to introducing the photocatalyst into the reactor, Mo@MgAl-LDH underwent two washes with ultra-pure water. In a typical experiment, Mo@MgAl-LDH (40 mg) was dispersed in 600 mL of ultra-pure water, and then the resulting suspension was added to the reactor. The reactor, equipped with a circulating water outer jacket, maintained a temperature of 25°C. The photocatalyst suspension was continuously stirred in the dark while high-purity N_2 was bubbled through the suspension at a flow rate of 300 mL min^{-1} for 5 min to achieve an N_2-saturated aqueous suspension. Subsequently, the reactor was irradiated under visible light, with continuous high-purity N_2 bubbling and stirring. At specific intervals, a sample of the reaction solution was withdrawn using a syringe and immediately filtered to remove any photocatalyst. The concentrations of NH_3 (as NH_4^+ formation) in each aliquot were quantified by ion chromatography (930 compact IC Flex, Metrohm). Quantification was based on standard calibration curves created by plotting peak area by ion chromatography versus NH_4^+ or NO_2^-/NO_3^- on centration. The O_2 evolution was recorded with a Hansatech Clark oxygen electrode (Hansatech Instruments, DW1/AD unit with an S1 electrode). The concentration of N_2H_4 was monitored colorimetrically using para-(dimethylamino) benzaldehyde. UV-vis absorption spectra of the colored complexes formed in the colorimetric tests were recorded on a Shimadzu UV-2550 UV-vis spectrometer.

The apparent quantum efficiency tests

AQE was evaluated through photoreactions conducted under laboratory conditions using a 300 W Xe lamp (PLS-SXE300DUV). The experimental procedure involved employing a volume of ultra-pure water (600 mL) as the reaction medium, in which Mo@MgAl-LDH (0.5 g) served as the photocatalyst. To maintain an inert atmosphere, the photoreactions were carried out under a continuous flow bubbling of N_2 gas (300 mL min^{-1}). Before introducing the photocatalyst into the reactor, the Mo@MgAl-LDH underwent two washes with ultra-pure water to ensure the removal of any impurities. To maintain a constant temperature of 25°C, the reactor was equipped with an outer jacket that facilitated the circulation of water. At specified intervals (30 min), a sample of the reaction solution was withdrawn from the reactor using a syringe, immediately followed by filtration to remove any remaining traces of the photocatalyst. The concentrations of NH_3 (present as NH_4^+) in each sample were quantified using ion chromatography (930 compact IC Flex, Metrohm).

The NH_3 production rate was calculated using the following equation (equation):

$$c\,(NH_3)\left(\text{mol g}^{-1}\,\text{h}^{-1}\right) = \frac{n\left(NH_4^+\right)}{m\,(\text{photocatalysts}) \times t\,(\text{illumination time})} \quad \text{(Equation 1)}$$

Where $n\,(NH_4^+)$ represents the number of moles of generated NH_3, m (photocatalysts) is the quality of the photocatalysts used in the reaction, and t (illumination time) is the illumination time.

The AQE at different wavelengths was determined using monochromatic filters with a bandwidth of ± 5 nm, and calculated as follows:

$$\text{AQE}\,(\%) = \frac{3 \times \text{the number of evoluted } NH_3 \text{ molecules}}{\text{the number of incident photons}} = \frac{3 \times [NH_3 \text{ formation (mol)}] \times N_A}{\frac{[\text{total input energy (W)}] \times [\text{time (s)}]}{h \times \nu}} \times 100 \quad \text{(Equation 2)}$$

Where [NH_3 formation (mol)] is the amount of substance for the generated NH_3; N_A and h are the Avogadro constant and Planck constant, respectively. The [total input energy (W)] can be calculated by (incident light intensity irradiation area); [time (s)] represents the irradiation time, while ν is incident light frequency.

Photocatalytic N_2 reduction cycling tests

The experimental conditions and procedures are consistent with the above tests. Photocatalytic NH_3 production cycling tests were measured through photoreactions carried out under laboratory conditions implementing a 300 W Xe lamp (PLS-SXE300DUV). The experimental procedure involved employing a volume of ultra-pure water (600 mL) as the reaction medium, in which Mo@MgAl-LDH (0.12 g) served as the photocatalyst. The photoreactions were carried out under a continuous flow bubbling of N_2 gas (300 mL min^{-1}) to maintain an inert atmosphere. Before putting the photocatalyst into the reactor, the Mo@MgAl-LDH was washed twice with ultrapure water to remove any contaminants. To keep the temperature constant at 25°C, the reactor included an exterior jacket that allowed water to circulate more easily. A syringe was used to take a sample of the reaction solution from the reactor at regular intervals (30 min), followed by filtering to eliminate any leftover photocatalyst traces. The quantities of NH_3 (as NH_4^+) in each sample were determined utilizing ion chromatography (930 compact IC Flex, Metrohm). After 12 h of reaction, the catalyst in the reaction solution is separated by centrifugation (12000 r/min). The obtained solid products were used for photocatalytic NH_3 production cycling tests under the same reaction conditions. Repeat this cycle three times.

Isotopic labeling experiments

To confirm that the observed NH_3 in the photocatalytic experiments originated from dissolved N_2, additional isotopic labeling experiments were conducted using $^{15}N_2$. In summary, these experiments took place in a stainless steel reactor featuring a circulating water outer jacket for temperature control and a quartz window at the top for light irradiation. The wet photocatalyst (30 mg) was uniformly dispersed in a quartz bowl in the reaction chamber, using 5 mL of ultra-pure water. Following the complete evacuation of the chamber utilizing a mechanical pump, individual $^{14}N_2$ gas or $^{14}N_2 + {}^{15}N_2$ (V:V = 1:1) mixed gas (100 mL) was injected into the chamber, and then the chamber was photo-irradiated for 12 h. After the photoreaction, the photocatalyst and reactor were infiltrated with 3 mL of ultrapure water. Subsequently, 1 mL of the reactor washings mixed with 0.2 mL of a phenol solution (1.2 g of phenol dissolved in 10 mL of a 95% ethanol/water mixture), 0.2 mL of a sodium nitroso ferricyanide solution, and 0.7 mL of a NaClO solution (comprising 2.5 mL of a 5 wt.% NaClO solution, 0.1 g of NaOH, and 2 g of sodium citrate in 10 mL of water). 2.1 mL of the mixed solution was transferred to a mass spectrometer bottle and analyzed by high-resolution electrospray ionisation mass spectrometry (Bruker Apex IV Fourier Transform Mass Spectrometer). The mass spectra qualitative detection of ammonia was referenced in our previous report.

Photoelectrochemical measurements

A CHI 660E electrochemical workstation was employed to conduct various electrochemical and photoelectrochemical measurements in a three-electrode cell. Florine-doped tin oxide (FTO) electrode uniformly coated with a photocatalyst was used as the working electrode, while a platinum foil and a saturated Ag/AgCl electrode served as the counter and reference electrodes, respectively. The aqueous Na_2SO_4 solution (1 mol L^{-1}) was regarded as the electrolyte. A slurry composed of 7.5 mg of catalyst, 1 mg of ethyl-cellulose, 0.5 mL of α-terpineol, and 1 mL of absolute ethanol mixture was prepared and dropwise applied onto the FTO electrode. Mott-Schottky plots experiments were conducted at a frequency (500, 1000, and 2000 Hz) in the dark.

Poisson equation can be solved to give the Mott-Schottky equation:[4]

$$\frac{1}{C^2} = \frac{2}{\varepsilon\varepsilon_0 e A^2 N_D}\left(V - V_{fb} - \frac{k_B T}{e}\right) \quad \text{(Equation 3)}$$

Where C and A are the interfacial capacitance and area, respectively, N_D is the number of donors, V is the applied voltage, k_B is the Boltzmann constant, T is the temperature, and e is the electronic charge. Therefore, a plot of $1/C^2$ against voltage should yield a straight line from which V_{fb} (flat band potential) can be determined from the intercept on the voltage axis. The value of N_D is determined from the slope with knowledge of ε and A.

Gibbs free energy calculations of nitrogen photofixation to ammonia

Photocatalytic NH_3 evolution has emerged as a promising strategy for nitrogen fixation employing earth-abundant water, a readily available and affordable H^+ source. Moreover, the possibility of using NH_3/O_2 fuel cells (with a theoretical potential of 1.17 V *vs.* NHE (normal hydrogen electrode)) as an alternative to H_2/O_2 cells (1.23 V *vs.* NHE)[5] has also spurred profound interest in the photocatalytic conversion of N_2 to NH_3. The process involves the oxidation of water by holes (h^+) (Equation 5) and the reduction of N_2 by electrons (e^-) (Equation 6), resulting in the formation of NH_3 utilizing sunlight illumination under ambient conditions (Equation 7). Furthermore, the sizable free-energy gain associated with the reactions of H_2O splitting (Equation 8).

$$2H_2O + 4h^+ \rightarrow O_2 + 4H^+ \ (1.23\ V\ vs.\ NHE) \quad \text{(Equation 5)}$$

$$N_2 + 6H^+ + 6e^- \rightarrow 2NH_3 \ (0.055\ V\ vs.\ NHE) \quad \text{(Equation 6)}$$

$$1/2N_2 + 3/2H_2O \rightarrow NH_3 + 3/4O_2 \ \left(\Delta G^\circ = +339\ kJ\ mol^{-1}\right) \quad \text{(Equation 7)}$$

$$H_2O \rightarrow 1/2O_2 + 4H_2 \ \left(\Delta G^\circ = +237\ kJ\ mol^{-1}\right) \quad \text{(Equation 8)}$$